Seasonal to intraseasonal variability of the upper ocean mixed layer in the Gulf of Oman

Estel Font[1], Bastien Yves Queste[1], and Sebastiaan Swart[1]

[1]University of Gothenburg

November 30, 2022

Abstract

High-resolution underwater glider data collected in the Gulf of Oman (2015-16), combined with reanalysis datasets, describe the spatial and temporal variability of the mixed layer during winter and spring. We assess the effect of surface forcing and submesoscale processes on upper ocean buoyancy and their effects on mixed layer stratification. Episodic strong and dry wind events from the northwest (Shamals) drive rapid latent heat loss events which lead to intraseasonal deepening of the mixed layer. Comparatively, the prevailing southeasterly winds in the region are more humid, and do not lead to significant heat loss, thereby reducing intraseasonal upper ocean variability in stratification. We use this unique dataset to investigate the presence and strength of submesoscale flows, particularly in winter, during deep mixed layers. These submesoscale instabilities act mainly to restratify the upper ocean during winter through mixed layer eddies. The timing of the spring restratification differs by three weeks between 2015 and 2016 and matches the sign change of the net heat flux entering the ocean and the presence of restratifying submesoscale fluxes. These findings describe key high temporal and spatial resolution drivers of upper ocean variability, with downstream effects on phytoplankton bloom dynamics and ventilation of the oxygen minimum zone.

Seasonal to intraseasonal variability of the upper ocean mixed layer in the Gulf of Oman

Estel Font [1], Bastien Y. Queste[1], and Sebastiaan Swart[1,2]

[1] Department of Marine Sciences, University of Gothenburg, Gothenburg, Sweden

[2]Department of Oceanography, University of Cape Town, Rondebosch, South Africa

Corresponding author: Estel Font (estel.font.felez@gu.se)

Key points:

- Ocean glider observations reveal mixed layer variability that cannot be explained by seasonal warming alone.
- Shamal winds dominate intraseasonal variability of the mixed layer in the Gulf of Oman.
- Submesoscale mixed layer eddies are responsible for 68% of the restratifying buoyancy flux in winter.

Abstract

High-resolution underwater glider data collected in the Gulf of Oman (2015-16), combined with reanalysis datasets, describe the spatial and temporal variability of the mixed layer during winter and spring. We assess the effect of surface forcing and submesoscale processes on upper ocean buoyancy and their effects on mixed layer stratification. Episodic strong and dry wind events from the northwest (Shamals) drive rapid latent heat loss events which lead to intraseasonal deepening of the mixed layer. Comparatively, the prevailing southeasterly winds in the region are more humid, and do not lead to significant heat loss, thereby reducing intraseasonal upper ocean variability in stratification. We use this unique dataset to investigate the presence and strength of submesoscale flows, particularly in winter, during deep mixed layers. These submesoscale instabilities act mainly to restratify the upper ocean during winter through mixed layer eddies. The timing of the spring restratification differs by three weeks between 2015 and 2016 and matches the sign change of the net heat flux entering the ocean and the presence of restratifying submesoscale fluxes. These findings describe key high temporal and spatial resolution drivers of upper ocean variability, with

downstream effects on phytoplankton bloom dynamics and ventilation of the oxygen minimum zone.

Plain language summary

Atmospheric forcings, such as wind and solar heating, and small-scale ocean processes (1-10 km; e.g., eddies, fronts, filaments) modify the properties and the structure of the water column near the surface. These processes regulate the surface layer, creating a well-mixed surface layer. The variation in these processes determine how the depth of this surface mixed layer changes through both time and space. This study investigates the variability of this layer during winter and spring in the Gulf of Oman using in situ observations and atmospheric data derived from models and observations. Episodic strong and dry winds from the northwest (Shamals) increase mixing and cause shorter-term variability of the surface mixed layer. Concurrently, we find that the small-scale ocean processes mainly shoal the mixed layer depth during winter. These processes are also important in determining the timing of the change from the deeper winter mixed layer to the shallower spring mixed layer, as we find a three-week difference between the two observed years. The observations illustrate previously unquantified processes in the region that can impact coupling between the atmosphere, surface ocean, and deep ocean, with consequences for regional marine ecosystems.

Keywords: Latent heat flux, Mixed layer depth, Restratification, Shamals, Submesoscale fluxes

1 Introduction

The circulation, upper ocean stratification, and associated biogeochemical cycles in the Gulf of Oman (GoO) exhibit seasonality primarily driven by the monsoon cycle (L'Hegaret et al., 2016; Pous, 2004). Atmospheric forcing is highly temporally variable, ranging from diurnal to interannual fluctuations, altering the structural and functional characteristics of the upper ocean and surface buoyancy forcing of the surface ocean (L'Hegaret et al., 2016). Turbulent and convective mixing processes, powered by wind stress and heat exchange at the air-sea interface, play a pivotal role in the formation of a neutrally buoyant and well-mixed surface layer. The characterization of the spatial and temporal variability of the mixed layer depth (MLD) and the upper ocean stratification is essential to developing a better understanding of the exchanges of air-sea fluxes (e.g. heat, freshwater, and carbon) and their further implications in the regional ecosystem (Lévy et al., 2007; Piontkovski et al., 2017). For instance, the rate at which the ocean and atmosphere exchange properties and transfer critical climate gasses into the deeper ocean is influenced by ocean stratification and the vertical scale of the mixed layer (ML) (Sabine et al., 2004; Schmidt et al., 2019).

The Arabian Sea hosts the thickest and most intense oxygen minimum zone (OMZ) worldwide, with concentrations below 1 μmol kg^{-1} throughout much of the region (Angel, 2017; Queste et al., 2018; Lachkar et al., 2019; Rixen et al., 2020). Recent studies confirm that the Arabian Sea OMZ is highly sensitive to changes in the upper ocean stratification and forcing, such as warming and changes in monsoon winds (Lachkar et al., 2018, 2019, 2020; Goes et al., 2020). The Arabian Sea has warmed throughout the last century (Kumar et al., 2009; Piontkovski & Chiffings, 2014). This increase in surface temperature and stratification led to important ecological and biogeochemical changes, such as a reduction in the ventilation of the subsurface and intermediate layers, producing an intensification and growth of the OMZ and pelagic denitrification (Piontkovski & Queste, 2016; Lachkar et al., 2019; Schmidt et al., 2019). To properly represent deoxygenation in global climate models and to determine the response of the OMZ to further changes in climate, we must have an accurate description of the surface layer, linking the atmosphere and the OMZ, is required.

Strong and consistent southwesterly winds sweep through the area during the summer SW monsoon, which reverse during the slightly weaker NE winter monsoon. The spring and fall intermonsoons are distinguished by a decrease in wind strength and a lack of a prevailing wind direction (L'Hegaret et al., 2016). Regional factors such as orographic effects can also cause wind speeds and directions to be slightly more variable over the marginal seas of the Arabian Sea (Aboobacker & Shanas, 2018). Shamals are extratropical climate systems characterized by strong northwesterly winds blowing over the region with varying frequency throughout the year (Reynolds, 1993; Aboobacker & Shanas, 2018). Along Oman's coast, Shamal winds have speeds up to 15 m s^{-1} (Chaichitehrani & Allahdadi, 2018). These dry and strong wind events cause dust storms, which reduce solar radiation and increase turbulent heat loss, resulting in uniquely high surface heat losses that often drive convective mixing in the upper ocean of the Persian Gulf and Red Sea (Senafi et al., 2019). Turbulent mixing alters the vertical and horizontal distribution of temperature, salinity, and other parameters like phytoplankton or dissolved oxygen, hence modifying the biogeochemical characteristics of the region (Piontkovski et al., 2017; Queste et al., 2018; Lachkar et al., 2020).

One-dimensional forcing processes can explain a significant part of ML variations (Niiler & Kraus, 1977; Price et al., 1978). However, horizontal processes related to fronts, eddies, and filaments can also alter upper ocean stratification. Mesoscale eddies are present and widely studied in the GoO (Reynolds, 1993; Pous, 2004) and there is evidence of the existence of submesoscale features that influence phytoplankton residence time in the euphotic region, growth rates, biogeochemical fluxes, and community structure (Lévy et al., 2018; Morvan et al., 2020). Ras al Hamra and Ras al Hadd capes in the GoO (Figure 1) have been found to be submesoscale eddy generation hotspots (Morvan et al., 2020). Small vortices and rapidly evolving small-scale density filaments and fronts characterize these submesoscale motions that develop over space and time (1-10 km, from hours to days). ML variability is directly influenced by submesoscale instabilities (Boccaletti et al., 2007; Fox-Kemper et al., 2008) and it has been shown that this process can alter the timing of the seasonal restratification (Mahadevan et al., 2010; du Plessis et al., 2017).

In this study, we look at two types of submesoscale processes. First, baroclinic instabilities that grow at the internal Rossby radius and can evolve to submesoscale-sized eddies known as mixed layer eddies (MLEs) (Boccaletti et al., 2007; Fox-Kemper et al., 2008). MLEs contribute to restratifing MLs by rearranging horizontal buoyancy gradients, associated with fronts, into vertical stratification through an ageostrophic secondary circulation, with upwelling on the lighter side of the front and downwelling on the denser side (Fox-Kemper et al., 2008). Second, we look at surface winds blowing down-front that can erode stratification by a cross-frontal Ekman buoyancy flux (EBF) (Thomas, 2005; Thomas & Lee, 2005). Advection from the denser side of the front to the lighter side forces convective instabilities, increasing dissipation within the ML by up to an order of magnitude more than wind-driven shear (D'Asaro et al., 2011). Contrary, up-front winds advect the lighter side of the front over the denser side, increasing the vertical stratification. Previous glider studies have demonstrated the importance of both MLE and EBF in enhancing or arresting upper ocean stratification at seasonal to intraseasonal timescales (e.g., Thompson et al., 2016; du Plessis et al., 2017, 2019; Viglione et al., 2018).

The aim of this study is to describe the evolution of MLD and stratification in the GoO. We use high-resolution underwater glider data, collected over both winter and spring, coupled with reanalysis datasets, to determine the impact of surface buoyancy forcing variability on the upper ocean. In addition, we estimate the role of submesoscale processes on the subseasonal variability of the ML by applying established parameterizations that scale MLE and EBF as equivalent heat fluxes.

2 Data and methods

2.1 Glider sampling

Two Seagliders (Eriksen et al., 2001) sampled continuously along an 80 km transect between 22.5ºN, 58ºE and 24ºN, 59ºE. Seaglider 579 (SG579) was deployed in March 2015 and sampled until the end of May 2015 (91 days) during the spring intermonsoon (Figure 1a). Seaglider 510 (SG510) was deployed with the same mission plan in mid-December 2015 and retrieved at the end of March 2016 (108 days) during the winter NW monsoon (Figure 1b). Each glider sampled the water column with a conductivity-temperature-depth sensor (CTD) at a sampling rate of 0.2 Hz. Temperature is corrected for sensor lag (τ = 0.6 s), and salinity is then corrected according to Garau et al. (2011).

Upcast data were compared to the following downcast to check for temperature bias caused by warming of the sensors during the communication phase at the surface between dives (Figure S1). Strong solar radiation warmed the glider and its sensors, causing an artificial rise in potential temperature during the first 40 m of the downcast measurements in spring up to 0.08±0.44 ºC. The deviation was also evident but weaker in winter (0.02±0.16 ºC). The bias in downcast upper ocean data produces fictitious results when observing lateral gradients, hence only upcast data are used in this study.

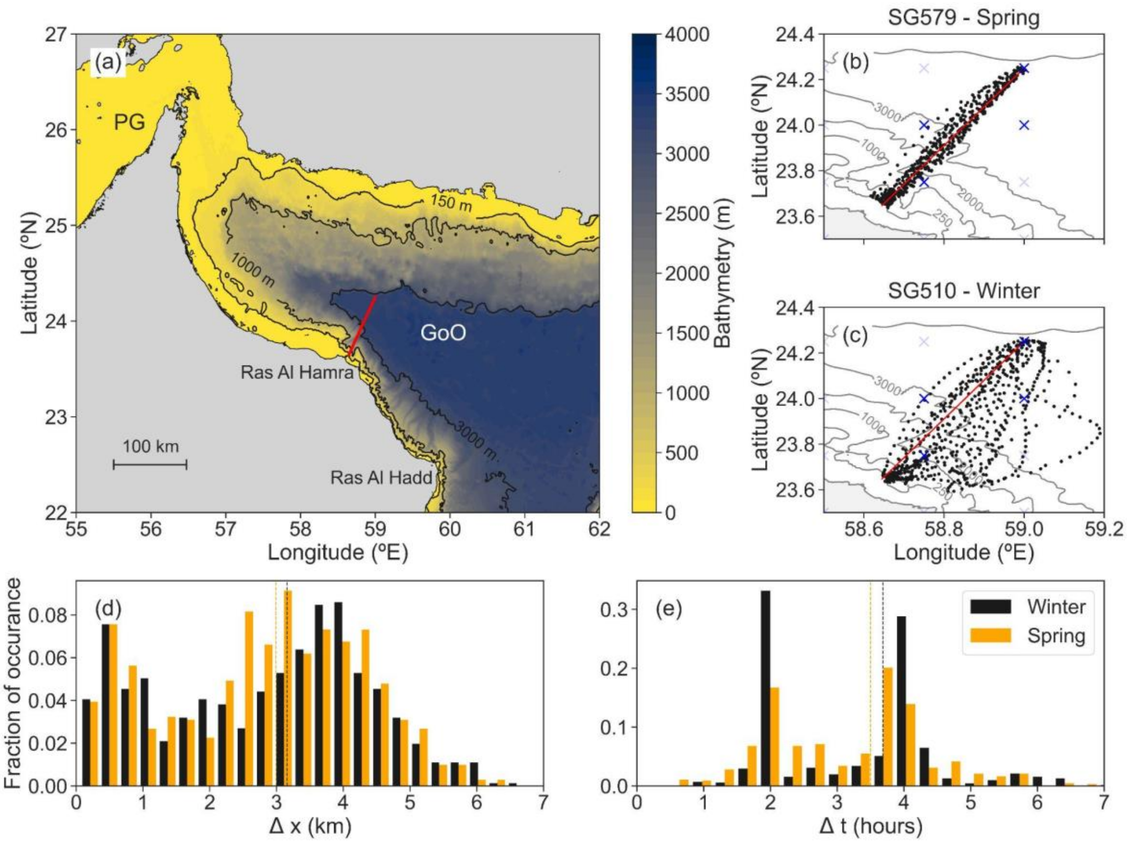

Figure 1. **Glider sampling.** (a) Bathymetric map (GEBCO, 2020) of the GoO. The red line defines the glider transect. (b) Spring and (c) winter Seaglider dive locations (black dots) and ERA5 reanalysis data points used (blue crosses). The solid grey line defines the coastline and isobaths are dashed The red line shows the same transect as in (a). (d) Along-track distance distribution between profiles and (e) temporal distribution between 3 km along-track grids from both campaigns.

A total of 712 profiles were used from the spring deployment and 815 profiles from the winter deployment. The horizontal and temporal resolution of a given dive is dependent on its maximum depth. Thus, the datasets have different spatial and temporal resolutions as the glider dives across the shelf from 150 m down to 1000 m over a few horizontal kilometers. The glider sampled at an average horizontal resolution of 0.42±0.51 km (0.70±0.59 h) onshelf, compared to 3.30±1.27 km (3.87±0.76 h) for the deeper profiles offshore, which is evidenced as shown in the bimodal distribution in Figure 1d. To compute comparable lateral and vertical gradients, the profiles were averaged on a 3 km along-track grid, which translates to a temporal resolution of 3.9±3.6 h in winter and 3.5±2.4 h in spring (Figure 1e). All data are binned in 0.5 m depth intervals. Data are linearly interpolated vertically and then along the 3 km along-track grid.

2.2 Satellite - reanalysis products

Data from ERA5, the fifth generation of the European Centre for Medium-Range Weather Forecasts (ECMWF) atmospheric reanalyses of global climate, are used in this study to assess the local surface buoyancy forcing and wind stress (Hersbach et al., 2020). ERA5 is highly accurate, representing the magnitude and variability of near-surface air temperature and wind regimes (Pokhrel et al., 2020). A 0.25º × 0.25º grid and hourly data provide high spatial and temporal resolution. To compare ERA5 time series to the glider observations, we use an hourly average of the four ERA5 points colocated with the glider's path (Figure 1).

Zonal and meridional wind components at a height of 10 m above the sea surface are used to compute wind speed (U), wind direction, and wind stress as

$$\tau = \rho_{\mathrm{air}} \cdot C_{\mathrm{d}} \cdot \mathrm{U}^2, \qquad [1]$$

where ρ_{air} is the air density and the drag coefficient $C_{\mathrm{d}} = 0.001\cdot(1.1+0.035\cdot U)$ (CERC, 2002). Moreover, sea surface temperature (SST) and dewpoint temperature at 2 m above the surface are used to compute the saturated specific air humidity at sea level (q_s) and the specific air humidity (q_a), respectively. Evaporation (E) and precipitation (P) rates are also used in the analysis. Net surface heat flux entering the ocean (Q_{NET} is computed through the sum of ERA5 flux products: solar radiation (Q_{SW}), net long-wave radiation (Q_{LW}), latent heat flux (Q_{L}), and sensible heat flux (Q_{S}). The sign convention used here is that a negative flux represents a heat loss from the ocean to the atmosphere.

The buoyancy flux through the surface (B) is used to determine the stability of the upper ocean and can be expressed as:

$$B = g \cdot \left[\frac{\alpha \cdot Q_{NET}}{\rho_0 \cdot c_p} - \beta \cdot S_A \cdot (E - P)\right], \qquad [2]$$

where g is the gravity constant, $\rho_0 = 1027$ kg m^{-3} is the reference density, c_{p} is the specific heat of seawater, S_{A} is the median absolute salinity between 10 and 15 m, α is the effective thermal expansion coefficient ($-\rho^{-1}\cdot(\partial\rho/\partial T)$), and β is the effective haline contraction coefficient ($\rho^{-1}\cdot(\partial\rho/\partial S)$). T and S represent *in situ* temperature and practical salinity respectively. Q_{NET} has units W m^{-2}, E and P have units m s^{-1}, and B has units m^2 s^{-3}.

The latent heat flux (Q_L) can be estimated from wind speed and air-sea humidity differences using the following bulk parameterization (Yu, 2009; B. P. Kumar et al., 2017):

$$Q_L = \rho_{air} \cdot L_e \cdot C_e \cdot |U - U_c| \cdot (q_a - q_s)\ , \quad [3]$$

where L_e is the latent heat of vaporization and is a function of sea surface temperature, expressed as $(2.501\text{-}0.00237\cdot\Theta)\cdot 10^6$ K, where Θ is the median conservative temperature between 10 and 15 m depth, and $C_e = 1.3\cdot 10^{-3}$ is the transfer coefficient of Q_L (Yu, 2009). We commit an error of up to 5% when taking C_e independent of wind speed, overestimating the Q_L loss by up to 8 W m^{-2}; we make this simplification to ensure linearity between U and q for later analysis. The surface current speed, U_c, is calculated through the surface drift of the glider. We neglect the contribution of U_c in Equation 3 as it is estimated to decrease Q_L by less than 3%, with surface current speeds up to 0.6 m s^{-1} (not shown).

2.3 Definition of the MLD

The MLD is defined using the threshold method with a finite difference criterion for each individual profile (Montégut et al., 2004). The specific criteria considered for the computation of MLD is

$$\sigma_0(10\, m) - \sigma_0(z) = 0.125\ kg\ m^{-3}, \quad [4]$$

where $\sigma_0(z)$ is the potential density at depth z and $\sigma_0(10\text{ m})$ is the potential density at 10 m depth. The reference depth is chosen to avoid the strong diurnal warming cycle in the top few meters. The threshold criterion is selected based on visual inspection of a representative sample of randomly picked profiles from both campaigns. Averaged observations between 10 and 15 m depth are used to compute ML properties in order to avoid biases linked to diurnal warm layer formation, internal wave processes, or larger salinity errors due to sensor thermal lag close to the pycnocline.

2.4 Horizontal buoyancy gradients

Buoyancy is determined using the formula

$$b = g\ \cdot\ (1 - \rho/\rho_0), \quad [5]$$

where g is the gravity constant and ρ_0 defined in Equation 2. Horizontal buoyancy gradients, b_x, are computed as the buoyancy difference between consecutive 3 km uniformly gridded profiles along-track (x-direction). Errors may be introduced as a result of the interpolation across non-uniform distances (i.e. different resolutions onshelf and offshelf). It is not possible to distinguish between the spatial and temporal components of the horizontal buoyancy gradients. Moreover, gliders generally underestimate b_x because they can only measure the full magnitude while diving perpendicular to the sampled front. Thompson et al. (2016) determined an averaged $1/\sqrt{2}$ underestimation of b_x when sampling a front at all possible angles and assuming mean buoyancy gradients are isotropic. The frontal flow direction is represented by the dive averaged current (DAC) direction (du Plessis et al., 2019). In this study, the glider underestimated the true buoyancy gradients by 69% based on the difference between the front direction and the glider dive direction (Figure 2). This value is comparable to the estimates in different ocean regions, which range between 51 and 71% (Thompson et al., 2016; du Plessis et al., 2019; Swart et al., 2020). Hence, we provide a statistical representation of the relative magnitude of the fronts, even though absolute calculations are biased low.

The relative influence of temperature and salinity on horizontal buoyancy gradients is quantified with the horizontal Turner angle (Tu), which is defined as

$$Tu = tan^{-1}(Rp), \qquad [6]$$

using the density ratio (Turner, 1973)

$$Rp \equiv \left(\alpha \frac{\partial T}{\partial x}\right) \cdot \left(\beta \frac{\partial S}{\partial x}\right)^{-1}, \qquad [7]$$

where $\frac{\partial T}{\partial x}$ and $\frac{\partial S}{\partial x}$ are the horizontal derivatives of temperature and salinity on the 3 km along-track grid data. Fronts in which Tu is positive are at least partially compensated, with $Tu > \pi/4$ indicating that temperature has a stronger impact on density than salinity. Fronts where $Tu < 0$ are anti-compensated in which salinity and temperature are acting constructively to create differences in density. For $Tu = \pi/4$, temperature stratification is fully compensated by salinity stratification. For $Tu = -\pi/4$, salinity and temperature contribute equally to the density stratification. Salinity stratification exceeds the contribution from temperature stratification when $-\pi/4 < Tu < \pi/4$, and temperature stratification dominates when $|Tu| > \pi/4$.

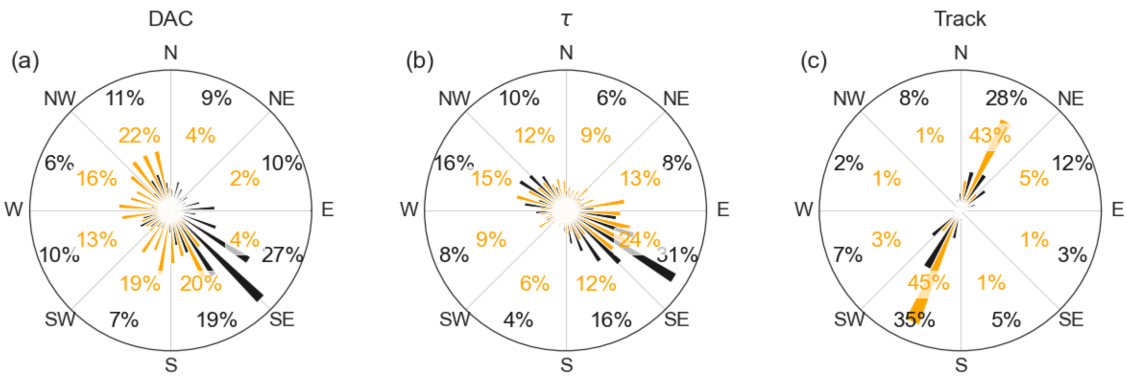

Figure 2. **DAC, wind stress, and glider trajectory direction.** (a) Direction of the dive averaged current (DAC) corresponding to the frontal flow direction. (b) Direction of the wind stress, τ. (c) Glider track direction. Winter distribution in black and spring in orange.

2.5 Submesoscale equivalent heat fluxes

Fox-Kemper et al. (2008) provide a parameterization of the restratification mechanism by MLEs, which has been used in other studies in terms of equivalent stratifying heat flux, Q_{MLE} (Mahadevan et al., 2012, du Plessis et al., 2017, 2019; Giddy et al., 2021). MLEs transform horizontal buoyancy gradients to vertical stratification, therefore Q_{MLE} depends on the strength of horizontal buoyancy gradients and MLD as:

$$Q_{MLE} = 0.06 \cdot \frac{b_x{}^2 \cdot MLD^2 \cdot c_p \cdot \rho_0}{f \cdot \alpha \cdot g}, \qquad [8]$$

where 0.06 is a coefficient determined by Fox-Kemper et al. (2008), b_x is the horizontal buoyancy gradient in the ML taken as the median value between 10 and 15 m, and $f = 5.94 \cdot 10^{-5}$ s^{-1} (the Coriolis parameter at 24 ºN). Note that Q_{MLE} always acts as a positive (restratifying) buoyancy flux.

Winds directed along a front promote mixing or restratification through a cross-frontal Ekman buoyancy flux (EBF), which advects water from the denser side of the front over the lighter side (mixing), or from the lighter to the denser side (restratification) (Thomas, 2005; Thomas & Lee, 2005). EBF processes can be quantified as an equivalent heat flux following:

$$Q_{EBF} = \frac{b_x \cdot \tau_Y \cdot c_p}{f \cdot \alpha \cdot g}, \qquad [9]$$

where b_x is defined as in Equation 8 and τ_y is the along-front component of wind stress. Wind stress is temporally collocated to the gridded glider data, and following du Plessis et al. (2019), τ_y is determined from the angle difference between the direction of the DAC (front direction) and the wind direction. τ_y is defined positive to the right of the glider's trajectory. Upfront (downfront) winds are defined when the along-track b_x and τ_y have the same (different) sign. Hence, negative values of Q_{EBF} represent a negative buoyancy flux, while positive values denote a positive buoyancy flux. For instance, a glider transiting northwards across a front from dense to light water ($b_x > 0$) and westerly winds ($\tau_y > 0$), promote a southwards Ekman transport (northern hemisphere), advecting light water on the denser side and resulting in restratification.

Submesoscale equivalent heat flux ($Q_{SMS} = Q_{MLE} + Q_{EBF}$) is determined by the competition between the restratification processes of MLEs, which are positive, and EBF, which can be positive or negative. Both Q_{MLE} and Q_{EBF} estimate how much surface heat flux would be needed in the ML to achieve equivalent restratification or mixing.

3 Results

3.1 A high resolution view of the ML seasonal cycle

Two glider datasets spanning the spring intermonsoon (SG579; March 2015 - May 2015) and winter monsoon (SG510; December 2015 - March 2016) present distinct regimes in the upper ocean stratification and ML properties. The winter monsoon exhibits a deep ML (79±19 m average before restratification) and a cooling of the ML waters from mid-December to mid-February of 1.59±0.24 ºC (Figure 3). During the spring intermonsoon, the effect of seasonal warming lightens the surface waters by approximately 2.5 kg m^{-3} throughout the three month period. This decrease in potential density (σ_0) is primarily driven by the near-persistent increase in conservative temperature (Θ) of 8.33±0.12 ºC over three months (Figure 3). This steadily increasing surface buoyancy shoals the ML to 16±7 m on average after restratification (Figure 3). Absolute salinity (S_A) in the ML fluctuates around 36.9±0.15 g kg^{-1}, before increasing slightly throughout spring by 0.20±0.02 g kg^{-1}, with two events of decreased salinity on 20 April 2015 and 19 May 2015 (0.15-0.20 g kg^{-1}).

Changes in σ_0 are mainly driven by variations in temperature in both seasons (70% of the time during winter and 87% in spring), evident in Figures 3e-f, where Θ and S_A are scaled to show equal contributions to changes in σ_0. Another characteristic feature in the region is the Persian Gulf Water outflow, which transports warm and salty water from the Persian Gulf that sinks after the Strait of Hormuz and flows southeastward as a shelf gravity current along the Omani shelf (Pous, 2004; Vic et al., 2015; L'Hegaret et al., 2016; Queste et al., 2018). It can be seen as a warmer and more saline water mass in the Θ and S_A sections around 200 m for both seasons when the glider transits off-shelf (Figures 3a-d).

Restratification of the upper ocean is defined by the formation of a buoyant ML from the surface during the change in regime from winter to spring (24 February 2016, 19 March 2015) (Figure 3). Surface warming lightens the upper layer, increasing the stratification (Brunt–Väisälä frequency, N^2) until the spring intermonsoon ML is formed (Figures 3e-f). At the end of February 2016, ML waters warmed by 2.02±0.15 ºC in two weeks (Figure 3g). A similar process can be seen in March 2015 when a 15 m ML is formed in two days above the deep winter ML (Figure 3h). After the formation of the spring ML, winter well-mixed surface water is trapped between the winter ML base pycnocline ($H_{25.19}$, σ_0 =1025.19 kg m^{-3} isopycnal) and the new pycnocline generated by buoyancy gain as stratification increases from the surface (Figure 3). This layering is present until the end of both time series.

The winter ML in 2016 exhibits intraseasonal instability, with episodes shoaling up to 40 m in a few hours, for example on 15 January and between 25 January and 1 February (Figure 3). When MLD is at its peak in mid-February, there are smaller variations of around 20 m. Furthermore, a few ML deepening events occurred during March 2016 (4, 12 & 21 March 2016) to a depth of 40 m. These mixing events promote lighter stratification at the beginning of the spring ML formation, compared to the strong signal in N^2 from the restratification period in 2015. During spring, three major deepening ML events up to 25-30 m generate a rise in ML density mostly occurring during periods where ML temperature variations present significant drops (4, 20 & 26 April 2015). These can be identified as periods of denser surface waters often resulting in ML density changes up to 0.50-0.25 kg m^{-3} (Figure 3h). Stratification is eroded from the surface facilitating mixing with cooler subsurface waters. Moreover, diurnal warm layers are noticeable in the diurnal periodicity of N^2 in the first meters, which are more prominent during spring and are constrained to the extent of the ML (Figure 3f). During the day, the ocean is stratified from the surface, while at night, the lower air temperature may lead to a formation of a colder layer of water, mixing the top few meters (Matthews et al., 2014).

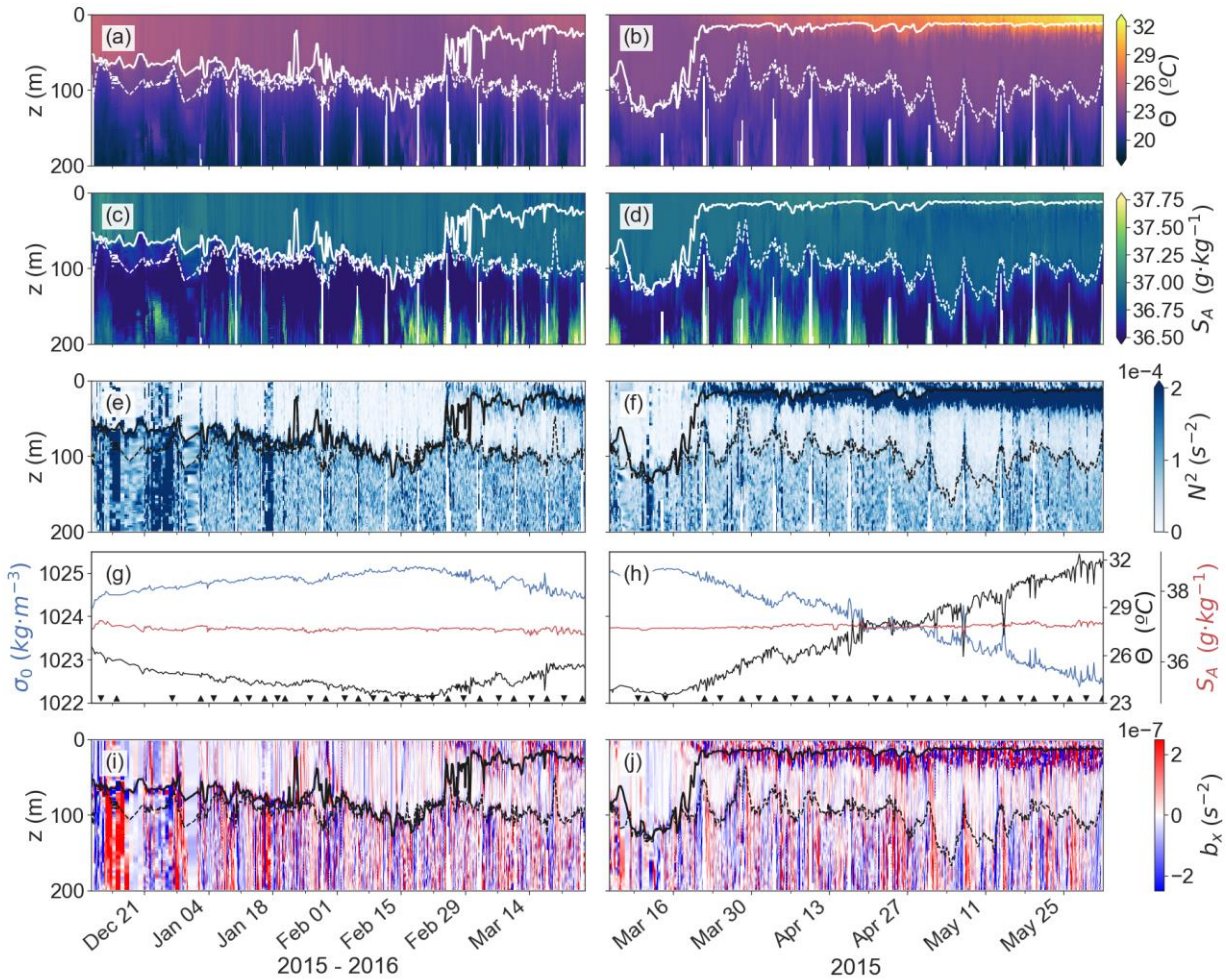

Figure 3. **Mixed layer properties and variability.** (a, c) Conservative temperature (Θ), (b, d) absolute salinity (S_A) sections, (e, f) N^2 sections for both seasonal datasets (winter: Dec 2015 to Mar 2016; spring: Mar to May 2015, respectively). (g, h) Time series of the median conservative temperature (Θ, black), absolute salinity (S_A, red), potential density (σ_0, blue) in the ML (average between 10-15 m), for winter (g) and

spring (h). Temperature and salinity are scaled to show equal contributions to changes in density. The limits of the transects are marked at the bottom of panels (g) and (h) with triangles (pointing up, onshelf; pointing down offshore). (i, j) Horizontal buoyancy gradients (b_x) in the upper ocean during winter (i) and spring (j). Solid black line denotes MLD with a 0.125 kg m^{-3} threshold criteria at 10 m reference depth. The dashed line denotes the isopycnal 1025.19 kg m^{-3} ($H_{25.19}$) defining the winter ML waters before the restratification.

The variability seen in the presented time series can be attributed to temporal fluctuations in the surface forcing, such as from varying heating or wind patterns. However, it may also be due to spatial differences in regional dynamics such as mesoscale eddies or smaller scale features like submesoscale fronts (see Section 3.3), as well as the displacement of the glider along the transect with a 4-7 days periodicity. The transect limits are labeled as triangles in Figures 3g-h to emphasize the spatial variability. For instance, the dense ML water peak during 10 March 2016 and 15 May 2015 and the subsequent transition around 18 March 2016 and 22 May 2015, respectively, correlate with the glider transiting the same location after seven days (Figures 3g-h). The MLD deepening on 20 April 2015 and later on 26 April 2015 is most likely caused by the glider sampling the same area six days later (Figure 3), as discussed in Section 3.2.1.

3.2 Surface forcing and buoyancy flux

Glider observations reveal a rich range of surface properties and stratification variability at subseasonal time scales and an overall strong seasonal cycle. Upper ocean stratification is studied through the sum of Brunt–Väisälä frequency (N^2) from the surface to the 1025.19 kg m^{-3} isopycnal, chosen because it defines the winter ML waters before the spring restratification ($\sum_z N^2$, Figures 4a-b). N^2 presents periodic peaks when the glider transits over the shelf (Figures 4a-b). There is a noticeable seasonal cycle in Q_{NET} with ocean heat gain generally in spring and heat loss in winter, which forces the upper ocean stratification and MLD seasonal pattern. In winter, strong wind events are more frequent and the general net cooling of the surface layer results in a deeper ML and less stratification ($\sum_z N^2$, Figures 4a-b).

Wind events exhibit frequencies of 4 to 7 days, with a prevailing northwesterly wind direction (Shamals) (Figures 4c-d). During spring time, warmer and lighter water is formed in the upper surface in response to the increasing solar radiation and a net heat flux entering the ocean ($Q_{\mathrm{NET}} > 0$). This positive heat flux creates a buoyant and shallow ML that traps the warm surface waters, increasing the stratification of the upper ocean and continuing to intensify throughout spring (Figures 4a-b). Evaporation dominates over precipitation (Figures 4c-d), which is enhanced by intense wind episodes throughout winter and spring. The exception occurs for two events on 3 & 9 March 2016 when strong wind-induced mixing likely offsets the effect of precipitation that promote restratification.

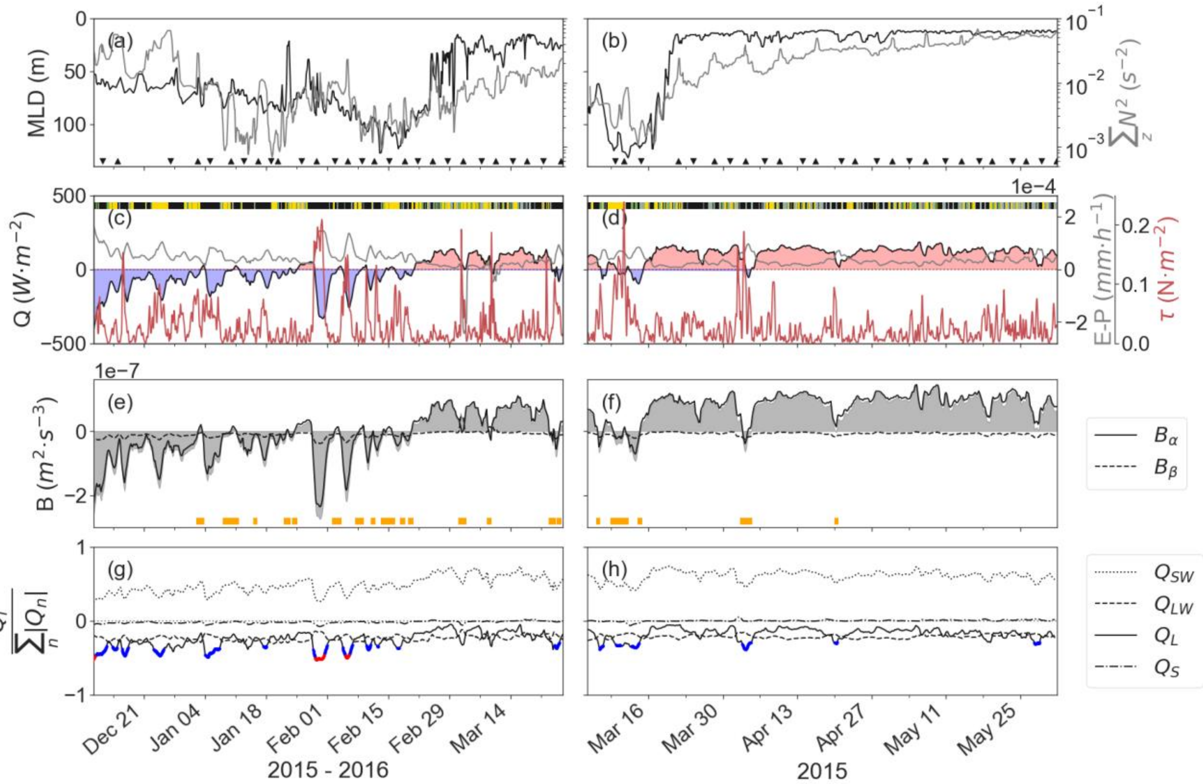

Figure 4. **Surface forcing.** (a, b) MLD (black) and upper ocean stratification ($\Sigma_{z=0}^{H_{25.19}} N^2$; gray) for winter (a) and spring (b). The limits of the transects are marked at the bottom with triangles (pointing up: onshelf; pointing down: offshelf) to highlight the spatial variability. (c, d) Surface atmospheric forcing: Q_{NET} ($Q_{\mathrm{NET}} < 0$: blue shading and $Q_{\mathrm{NET}} > 0$: red shading), $E-P$ (black solid line), and wind stress (τ, red line) for winter and spring, respectively. Wind direction is marked in the four-colored line (refer to the wind rose in Figure 5) as northwesterlies (black), northeasterlies (grey), southeasterlies (yellow), and southwesterlies (green). (e, f) Buoyancy flux, B, in gray shading and

thermal component (B_α, solid line) and haline component (B_β, dashed line). Orange markers indicate when $B_\alpha < B_\beta$. (g, h) Contribution of heat flux components to Q_{NET}: Q_{SW} (dotted), Q_{LW} (dashed), Q_L (solid), and Q_S (dash-dotted). The Q_L contribution is marked in blue when the daily average latent heat loss events exceed 1σ below the mean for both seasons (i.e., $Q_L < -166$ W m^{-2}) and in red when exceeding 3σ below the mean (i.e., $Q_L < -295$ W m^{-2}).

The buoyancy flux, B, determines the stability of the upper ocean, and moreover, it is possible to determine whether the thermal (B_α) or haline (B_β) component is the main contributor (Equation 2). Heating and precipitation cause the water column to restratify (positive B), while evaporation and heat loss promote buoyancy loss and mixing (negative B). The error in Q_{NET} propagates into B as $\pm 3.5 \cdot 10^{-9}$ m^2 s^{-3} in winter and $\pm 2.6 \cdot 10^{-9}$ m^2 s^{-3} in spring. B is mostly driven by the thermal term (B_α), with a few exceptions (orange rectangles, Figures 4e-f) during a change of sign in the thermal term or during strong precipitation events, such as the drops on 3 & 9 March 2016. B has episodic falls throughout the winter monsoon, resulting in the upper ocean losing buoyancy and contributing to unstable conditions (Figure 4e). These periods coincide with heat loss events mainly caused by wind (Figures 4c-d). During the restratification, B turns positive following the trend in Q_{NET}, changing the regime and promoting the spring ML formation (Figures 4e-f). During the spring intermonsoon, the upper ocean gains buoyancy ($B > 0$), contributing to stable conditions (Figure 4f). A few exceptions promote deepening of the MLD when there is no buoyancy gain (04 & 20 April 2015). These events are caused by wind-driven heat loss and strong evaporation ($E-P > 1$ mm h^{-1}).

Heat flux variability drives B and is the main contribution to the stratification of the upper ocean and MLD evolution. We decompose Q_{NET} in the contribution of each component to explain seasonal and intraseasonal variability. The seasonal cycle is primarily caused by a gradual increase in Q_{SW} input from winter to spring as well as fewer and weaker Q_L events in spring (Figures 4g-h). In winter, Q_{SW} into the ocean is about 100 W m^{-2} less than during the spring intermonsoon. The mean Q_{SW} increased from 181±26 W m^{-2} in winter to 286±26 W m^{-2} in spring. The mean Q_L was -115±73 W m^{-2} in winter and -82±44 W m^{-2} in spring. Q_{LW} and Q_S terms have a relatively constant contribution to Q_{NET} during the studied periods (Figures 4g-h), varying by at most 50 W m^{-2}. Notably, Q_{NET} variability is primarily driven by episodic Q_L loss several times per month (Figures 4g-h). Each event results in Q_{NET} loss in winter up to -437±14 W m^{-2}. This can also occur in spring, albeit less frequently and with lower intensity (Q_{NET} loss up to -115±26 W m^{-2}).

The restratification of the upper ocean is characterized by the formation of a shallow ML and a steady increase in stratification (N^2) due to atmospheric forcing at the end of the winter and the beginning of the spring (Figures 4c-d). After losing heat during the winter monsoon, heat enters the ocean mainly through an increase in Q_{SW}. As wind strength decreases (τ < 0.05 N m^{-2}), Q_L contribution to heat decreases (Figures 4 & 5), reducing wind-driven mixing. The timing of the springtime restratification differs by three weeks between the two years (24 February 2016 vs. 19 March 2015), as defined by a shift in the sign of Q_{NET}. Furthermore, while the 2015 restratification shows a strong N^2 signal after the spring ML formation (Figure 3f), the 2016 restratification shows a less strong stratification of the surface layer within the first two weeks after restratification (Figure 3e), owing to three significant Q_L events eroding it and promoting mixing with the cold winter water below (Figure 4f).

3.2.1 Episodic ML deeping driven by latent heat loss

Latent heat loss events are evident in the time series throughout winter, with decreasing frequency and intensity in spring (Figures 4g-h). The most extreme heat loss events in this region are emphasized in Figures 4g-h in blue when the daily averaged latent heat loss exceeds 1 standard deviation (σ) below the mean for both seasons (i.e., Q_L < -166 W m^{-2}) and in red when exceeding 3σ below the mean (i.e., Q_L < -295 W m^{-2}). Each latent heat loss event resulted in a drop in Q_{NET}. The most prominent event in winter on 28 January 2016 (Q_{NET} = -367±23 W m^{-2}, Q_L = -437±14 W m^{-2}) was reinforced by a loss in Q_S due to cooler air (~4 ºC air-sea temperature differences, Q_S = -56±4 W m^{-2}). After the spring ML formation in 2015, increased Q_{SW} compensates for Q_L events, preventing strong periods of negative Q_{NET} , with the exception of the 02 April 2015 event (Figure 4d).

The effects of these events on the MLD are different. The event with Q_L larger than 3σ on 28 January 2016 reduced N^2 as the ML deepened (Figure 4a), whereas in the following event one week later, no fluctuation in the ML were observed. Previous to these large latent heat loss events, on 18 January 2016 there was a restratification event when the ML shoaled to 25 m that can not be explained through surface forcing fluxes alone. In spring 2015, both events below 1σ in Q_L in April eroded the strong surface stratification, deepening the ML to below 20 m (Figure 4b). Furthermore, there was a ML deepening event one week after the Q_L peak on 20 April 2015 that was not accompanied by any measured surface forcing. This could be attributed to spatial variability. The deepening of the ML due to the effect of the Q_L drop on 20 April 2015 may have lasted for a week and when the glider traveled through the same spot one transect later, the deeper ML was still appreciable (26 April 2015).

We further analyze the drivers of extreme Q_L loss events. Q_L events 1 to 3σ above the average occur during high wind episodes, U, and large air-sea humidity differences ($\Delta q = q_a - q_s$). Interestingly, these events are strongly correlated with northwesterlies (Figures 4 & 5). Q_L isolines, computed using Equation 3, are used to locate the extreme latent heat loss events (Figure 5). The prevailing wind directions in the region are NW and its reversals from the SE (73% of the time during winter; 63% during spring). Specifically, between W and N (270º-360º), accounting for 47% in winter and 36% in spring (Shamal winds) (Figure 2b). Shamals are also the most intense and driest winds impacting the region, predominantly in winter, and present values higher than the annual climatological average (Figures 4 & 5a). This combination triggers the most extreme heat loss events, resulting in both convective and turbulent mixing in the upper ocean. In spring, the intensity of Shamal winds decline, resulting in fewer and weaker Q_L loss events compared to the winter monsoon. Despite this, the Shamals remain the primary drivers of high heat loss during spring due to their drier nature. Episodic SE wind events occur in both seasons, with varying effects on latent heat loss. Two episodes of substantial heat loss when moderate dry winds are blowing from the SE are found during winter on 25 December 2015 and 17 February 2016 (Figure 4d). The strongest winds in spring are southeasterlies, which present a distribution that is higher than the climatological yearly mean (Figure 5b). However, these winds have a higher humidity rate and therefore do not cause significant heat loss (10 March 2015).

Transitional winds from the NW and SE between reversals are generally light and humid and thus do not conduct heat loss.

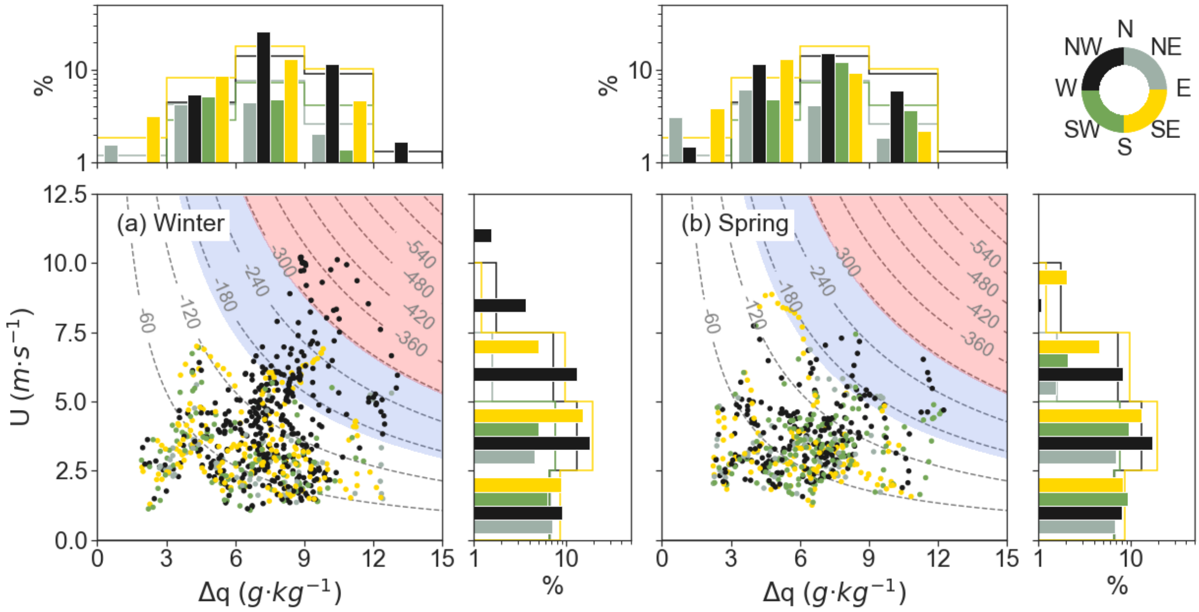

Figure 5. **Latent heat flux as a function of wind speed and humidity gradients.** Four-hourly air-sea humidity difference (Δq) vs. wind speed (U; ERA5 reanalysis) from winter (a) and spring (b). The scatter plots are colored by wind direction: northwesterlies (black), northeasterlies (grey), southeasterlies (yellow), and southwesterlies (green). Q_L isolines computed using Equation 3 are shaded in blue when heat loss events exceed 1σ below the mean for both seasons (i.e., Q_L < -166 W m^{-2}) and in red when exceeding 3σ below the mean (i.e., Q_L < -295 W m^{-2}). Top (side) histograms show the Δq (U) distribution of the hourly ERA5 datasets in filled bars and the climatological yearly mean using bar outlines (both colored by wind direction).

3.3 Submesoscale processes

3.3.1 Seasonal horizontal buoyancy gradients

Along-track buoyancy gradients (b_x) within the surface mixed layer cannot be distinguished between the temporal and the spatial component. We posture that in winter, horizontal buoyancy gradients in the ML are spatially driven ($\partial b/\partial x >> \partial b/\partial t$), given little evidence for temporally-induced variability. Conversely, during spring, the stronger diurnal cycle signal and shallow MLD provoque a temporally-dominated horizontal buoyancy gradients ($\partial b/dt >> \partial b/\partial x$). Seasonally, the weakest b_x are found in the winter ML with an enhancement occurring in spring ML (Figures 3i-j). Expectedly, b_x are amplified at the base of the ML, which is likely an artifact of internal wave processes vertically displacing the pycnocline and the glider sampling the pycnocline at somewhat variable depths over space and time (Figures 3i-j). The ML distribution of the b_x indicates an overall seasonality (Figure 6a). The upper limit of the winter b_x distribution is lower than the spring one, even after accounting for the glider sampling underestimation of 69% (see Section 2.4) (Figure 6a). Only 16% of the horizontal buoyancy gradients exceed 10^{-7} s^{-2} during winter, compared to 38% of the profiles during spring (Figure 6a).

The horizontal Turner angle (Tu) is computed to quantify the relative effect of temporal and spatial variations (horizontal gradients) of ML temperature and salinity on the horizontal density (buoyancy) gradients (see Section 2.4, Figure 6b). The distribution of Tu determines that horizontal temperature gradients have a major impact on density fronts than salinity gradients (distributions shifted to $\pm\frac{\pi}{2}$). We observe more frequent and stronger thermally-driven gradients during spring than during winter. The larger amplitudes observed in the spring b_x are likely driven by the presence of diurnal warm layers, given the stronger contribution of temperature variation in the density gradients in spring (Figure 6b). Thus, the spring b_x may be controlled by the temporal signal and not be representative of the spatial submesoscale fronts and cannot be used to determine equivalent submesoscale heat fluxes.

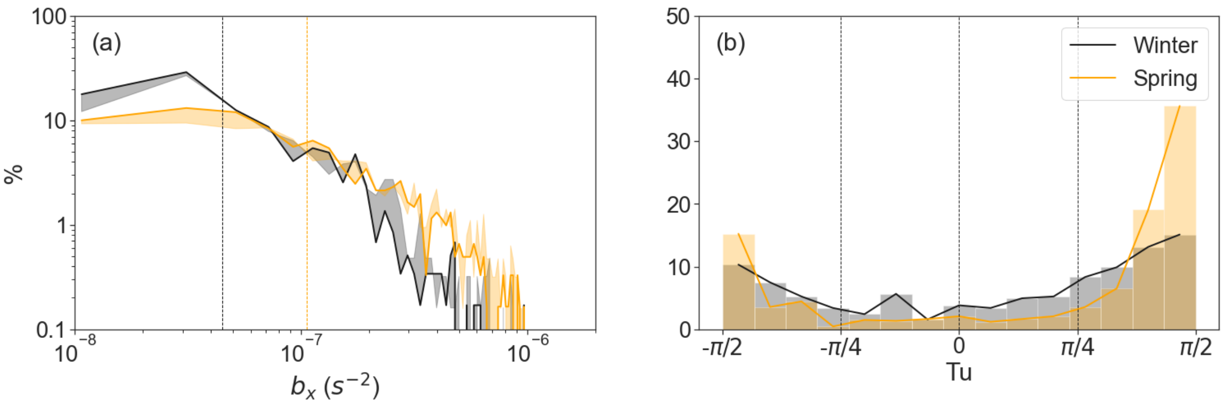

Figure 6. **Horizontal buoyancy gradients.** (a) Seasonal distribution of the median horizontal buoyancy gradients (b_x) between 10 and 15 m in winter (black) and spring

(orange). The shading represents the underestimation in the horizontal buoyancy gradient by 69%. Vertical lines in (a) show the median value of b_x for each season. (b) Horizontal Turner angle (*Tu*) distribution in winter (black) and spring (orange).

3.3.2 Wind-front alignment

The ML horizontal buoyancy gradient and the wind stress component aligned with the front are required to compute Q_{EBF} (see Section 2.5). In winter, the frontal flow direction, represented by the DAC direction, is predominantly between 90º and 180º, accounting for 46% of the profiles, whereas in spring, it is more widely distributed, with a predominant westerly component (Figure 2a). The wind direction is dominant along the NW-SE axis (73% during winter and 63% during spring) (Figure 2b). The along-front wind stress component is determined as the angle difference between the front and wind direction. In winter and spring, the median misalignment between DAC and wind direction are 42º and 60º, respectively. The wind-front alignment is evenly distributed between down and upfront. Down-front winds are present during 55% (50%) of winter (spring) time. The coherent alignment of winds and frontal direction promotes the occurrence of along-front winds, as well as the perpendicularity between the glider trajectory and the DAC (Figure 2c) leads to a good estimation of the horizontal gradients (see Section 2.4).

3.3.3 Submesoscale-driven fluxes in winter and spring

The length scale for submesoscale flows to develop in the surface layer is defined by the internal Rossby radius ($Lr = N \cdot H / f$), where N is the buoyancy frequency in the ML, H is the MLD, and f is the Coriolis parameter (Boccaletti et al., 2007). The median internal Rossby radius during winter and restratification is 4.7±1.6 km, indicating that the dataset is suitable for submesoscale analysis since we sample at scales smaller than Lr (3 km) (Boccaletti et al., 2007). In contrast, the median internal Rossby radius in spring is 2.5±1.1 km due to shallower MLD, indicating that the sampled resolution is insufficient to perform a submesoscale analysis in the spring dataset only (Boccaletti et al., 2007). Therefore, this section is focused on the contribution of submesoscale flows to changes in ML deepening and shoaling by restratification during winter up until the transition to spring. As described in Section 2.5, the estimated submesoscale fluxes (EBF and MLE) are represented as equivalent heat fluxes, comparable directly to surface heat fluxes. Negative values of Q_{EBF} represent a negative buoyancy flux, while positive values denote a positive buoyancy flux. Q_{MLE} is represented as a positive flux only given that MLEs act to vertically rearrange buoyancy.

Short temporal variability seen in the ML that cannot be explained by surface forcing could be explained by the submesoscale equivalent fluxes. Q_{SMS} events have the potential to dominate the total heat flux contribution and even reverse the sign of surface heat fluxes. The two case studies in Figure 7 indicate a direct effect of the Q_{SMS} on the MLD. Deep MLD and strong horizontal buoyancy gradients promote restratification via Q_{MLE}, reversing the Q_{NET} sign and resulting in a shallow MLD around 30 m during Case 1 (C1; Figure 7). The frontal structure crossed by the glider is seen in the SST map (Figure 7j). Furthermore, as wind stress is low (Figure 7h), wind turbulent mixing is unlikely to counteract MLE restratification produced by MLE. In contrast, Case 2 (C2) shows a strong Q_{EBF} event, when the horizontal buoyancy gradients and along-front winds ($\tau_y > 0$, right of the glider track) are large and act to stabilize or destabilize the ML, together with a restratifying contribution by Q_{MLE} (Figures 8k-n). Shamal winds blowing to the SE promote the advection of water through Ekman transport to the SW. On the 29th of January, the glider transits across a front, capturing the restratification promoted when lighter water was advected over the denser side of the front ($Q_{EBF} > 0$). At the end of the day, the glider crossed to a denser region, which resulted in MLD deepening due to the Ekman transport of denser over lighter water, promoting convection ($Q_{EBF} < 0$). After the 30th of January, the glider transited to a lighter region, resulting in $Q_{EBF} > 0$ accompanied by large Q_{MLE}, resulting in shoaling the MLD shallower than 50 m. No frontal structures were found afterwards, and the general winter surface cooling deepened the MLD again to 100 m (Figure 7k).

On average, winter submesoscale fluxes restratify the upper ocean. Q_{SMS} increase buoyancy 66% of the time during winter. When Q_{SMS} is positive, Q_{SMS} accounts for 68% of the total positive net heat flux budget $(\sum(Q_{NET} + Q_{SMS}) > 0)$. Submesoscale fluxes can reverse the sign of surface heat fluxes up to 11% of the time through a restratification flux by Q_{MLE} and positive Q_{EBF}, both of which oppose buoyancy loss. We expect the effect of Q_{MLE} to be larger during winter due to the deeper MLDs enhancing the available potential energy in the ML, and hence the capacity for MLEs to slump under gravity and to restratify the water column (Boccaletti et al., 2007). Q_{MLE} is largest when the MLD is deepest, with periodic spikes up to 800 W m^{-2} that promote restratification and result in shoaling of the ML (i.e. C1-24 January 2016 & C2-28 January 2016; Figure 7). Q_{EBF} contributes to restratification ($Q_{EBF} > 0$) 45% of the time, although it only accounts for the 15% of the positive Q_{SMS}, compared to 85% contribution of the MLE. Q_{SMS} account for the 21% of the total negative net heat flux budget ($\sum(Q_{NET} + Q_{SMS}) < 0$).

Seasonal warming of the ML causes a rise in stratification from winter to spring. According to our observations, springtime restratification rapidly shoals the ML from deeper than 100 m to 30 m in a matter of days. In 2016, when Q_{NET} changed sign and started adding buoyancy to the upper ocean, large periodic fluxes of Q_{MLE} during deep MLD indicated Q_{MLE} may be critical in supporting the stratification through thermal buoyancy gain. Conversely, horizontal buoyancy gradients were weaker during the 2015 restratification, resulting in lower Q_{MLE} estimates (< 100 W m^{-2}). Both restratification periods were accompanied by a weakening of the wind stress to less than 0.03 N m^{-2}, which contributed to a reduction in Q_{EBF} (to < 100 W m^{-2}) and a decrease of wind turbulent mixing.

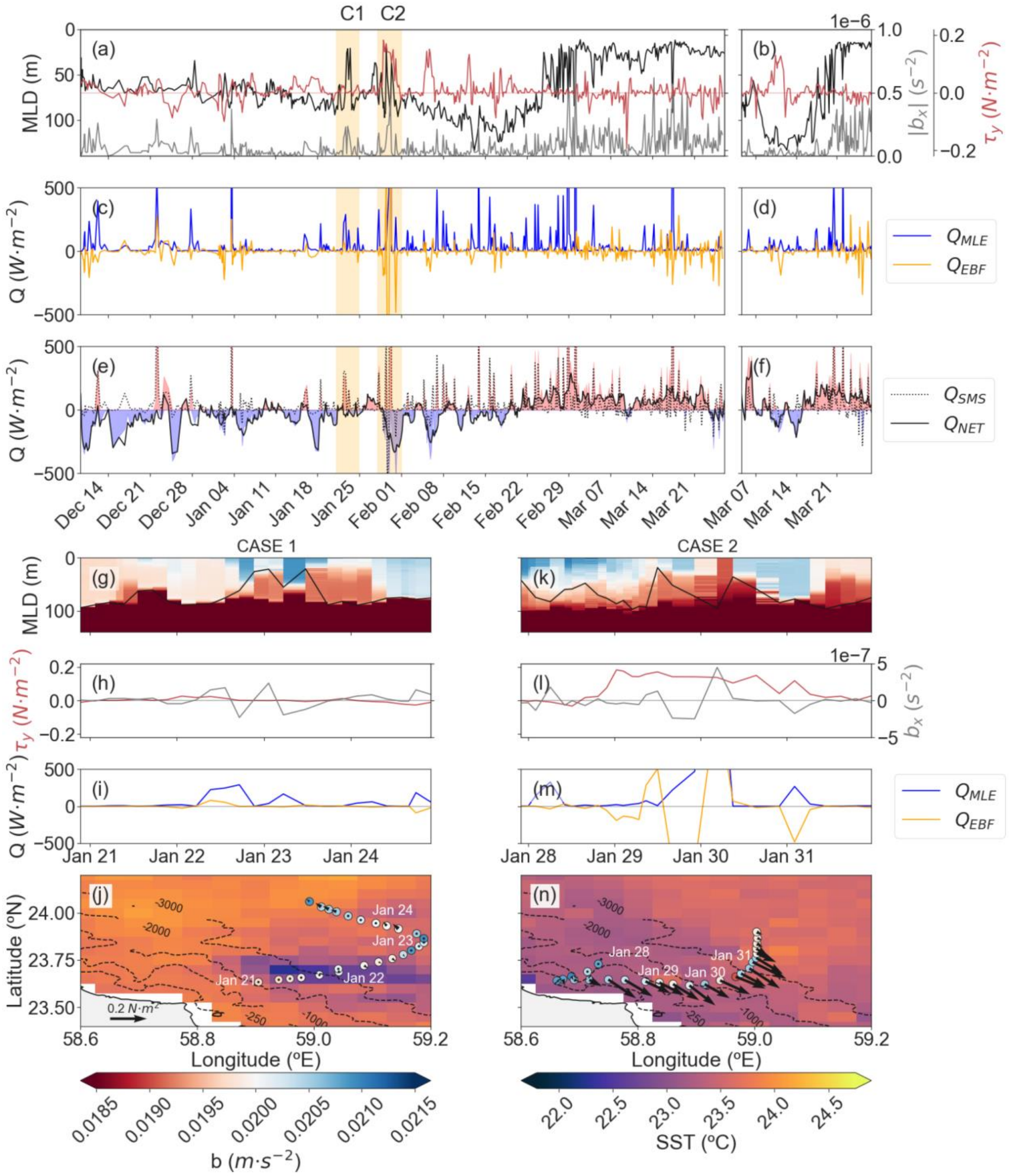

Figure 7. **Submesoscale equivalent fluxes**. The first column corresponds to 2016 winter and restratification and the second column is the 2015 spring restratification. (a, b) MLD (black), along-front wind stress (τ_y, red), where positive values indicate to the right of the glider trajectory and absolute horizontal buoyancy gradient, ($|b_x|$, gray). (c, d) Q_{MLE} (blue) and Q_{EBF} (orange). (e, f) Submesoscale fluxes ($Q_{SMS} = Q_{MLE} + Q_{EBF}$) in dotted line and net heat flux (Q_{NET}) in black solid line. The colored shading shows the total net heat flux ($Q_{SMS} + Q_{NET}$) in red (blue) when positive (negative). The yellow shading marks the two case studies (C1 & C2) that are zoomed in the Case 1 and Case 2

panels below. (g, k) Sections plots of buoyancy and MLD. (h,l) τ_y (red) and b_x (gray). (i, m) Q_{MLE} (blue) and Q_{EBF} (orange). (j, n) Trajectory of the glider colored by buoyancy on SST map on 23 and 29 January midday (SST from GHRSST L3C global sub-skin SST with 6 km resolution (EUMETSAT/OSI SAF, 2016) and isobaths (GEBCO, 2020). The arrows show the wind stress magnitude and direction.

4 Discussion

4.1 Surface flux contribution to ML variability and restratification

The seasonal evolution of MLD and restratification in the GoO is mainly driven by surface heating (positive Q_{NET}). Overall, the observed variability in MLD suggests a strong seasonality regulated by atmospheric forcing, such as incoming solar radiation, winds, and freshwater flux (Kumar & Narvekar, 2005). Suneet et al. (2019) demonstrated that air-sea fluxes contribute the most to the ML heat budget in the Arabian Sea. The surface heat budget is characterized by winter net heat loss and spring net heat gain due to an increase of Q_{SW}, which drives a positive buoyancy flux in the upper ocean, resulting in different stratification regimes between seasons (Figures 3 & 4). Temperature drove density changes 70% of the time during winter and 87% during spring (Figures 3 & 7). The combined effects of reduced Q_{SW} and evaporation in winter, under the influence of dry and intense Shamal winds that promote heat loss through turbulent fluxes, cool the upper layers of the GoO, as evidenced by the ML temperature evolution (< 24.5 ºC). At the ocean surface, buoyancy loss during winter months ($-3.65\pm0.3 \cdot 10^{-8}$ m^2 s^{-3}) induces vertical convection that erodes the stratification and deepens the ML to 79±19 m (Figure 4). During the spring intermonsoon, weaker winds and stronger incoming solar radiation result in an average buoyancy gain of $(8.2\pm0.3)\cdot10^{-8}$ m^2 s^{-3} and the formation of a shallow, warm, and strongly stratified ML that shoals to 16±7 m between March and May 2015. The weaker but steady winds (~5 m s^{-1}) blowing during spring are unable to erode the stratification and induce mixing of subsurface waters with the surface waters. Stable atmospheric conditions combined with a shift in Q_{NET} regime result in the creation of a shallow ML above the winter mixed waters. The restratification process is vital to biogeochemical cycling in the region (Lévy et al., 2007; Piontkovski et al., 2017). The timing and intensity of restratification can influence the biological evolution of the system during spring.

The high temporal resolution of this dataset reveals the impact of short and strong synoptic events on the upper ocean. Convective instability caused by buoyancy loss and wind-driven turbulence can explain the subseasonal MLD variability at relatively short timescales (1-3 days, Figure 3 & 4). Our observations reveal consistent signatures in the ratio between the heat flux components (Q_{LW}, Q_{L}, Q_{S}) and net cooling ($Q_{NET} < 0$) for the various intraseasonal events. In winter, Q_{L} accounts for 66% of heat loss, Q_{LW} accounts for 29%, and Q_{S} accounts for 5%. In spring, Q_{LW} contributes slightly more (35%) and Q_{S} slightly less (2%), while Q_{L} remains relatively constant (63%). Spring events are distinguished from winter events by the greater contribution of Q_{LW}, as well as the higher Q_{S} loss in winter due to stronger winds and colder air, resulting in larger air-sea temperature gradients. These observations are comparable to those found by Senafi et al. (2019) in the Persian Gulf and the Red Sea (Q_{LW}, Q_{L}, Q_{S}: winter 54-58, 23-30, 16-19% and spring: 58-61, 34-39, 3-5%). The Persian Gulf and the Red sea are semi-enclosed basins with extreme salinity and water temperature that experience larger temperature gradients between the atmosphere and the sea. The topographic characteristics of these basins can explain the greater contributions of Q_{S} in winter relative to the GoO. The main driver of heat loss in the GoO is Q_{L}, in agreement with model studies (e.g. Montégut et al. (2007) in the Arabian Sea) and its contribution to the total heat loss is similar between seasons.

Transient Q_{L} events are forced by intense wind speed events, which present significant air-sea humidity differences and show a clear signal correlated to the wind direction. The wind distribution during the studied periods reflects those measured by Aboobacker & Shanas (2018) and Chaichitehrani & Allahdadi (2018), with a predominance of northwesterly winds (Shamals) and their reversals. This study confirms that Shamal events, which are characterized by strong and dry winds from the NW, are the main drivers of surface heat loss and can alter the stratification and extent of the ML over short time scales (1-3 days). For instance, these events in spring are found to reduce the upper ocean stratification and deepen the ML from 20 m to 40 m (Figure 4). Aside from these Shamal events, sparse SE strong wind events occur in both seasons, triggering intense and sporadic latent heat loss (e.g. 16 February 2016 in Figure 6), though they are often associated with more humid air masses, reducing the potential heat loss.

4.2 The role of submesoscale processes

The observed magnitude and variability of ML evolution and the timing of restratification cannot be entirely explained by surface forcing alone. The high spatial resolution provided by the glider observations revealed submesoscale buoyancy fronts within the ML that had the potential to arrest or promote mixing. The equivalent submesoscale fluxes estimated in this study primarily contribute to stratifying the winter ML through both MLEs and EBF via upfront winds, contributing approximately 68% of the total positive heat budget ($\sum(Q_{NET} + Q_{SMS}) > 0$) and opposing surface cooling 11% of the time. Negative Q_{EBF} is important during certain periods and acts to enhance convective mixing that erodes the base of the ML. During the presence of buoyancy fronts in the ML, downfront winds enhance a destratifying EBF, which can erode upper ocean stratification and deepen the ML.

Prior studies in other regions have highlighted the importance of submesoscale processes promoting restratification through MLEs and wind-front interactions, resulting in a delay of the springtime ML shoaling (Mahadevan et al., 2012; du Plessis et al., 2019). Mahadevan et al. (2012) determined that the main contribution to stratification is driven by the seasonal Q_{NET} sign change and argued that restratification by MLEs before positive Q_{NET} causes a significant shift in the timing of the spring bloom in the North Atlantic. In the Southern Ocean, du Plessis et al. (2017) determined that MLEs increase stratification during spring, contributing to the surface heating by radiation. Meanwhile, a destratifying EBF can delay springtime restratification (du Plessis et al., 2019). Mahadevan et al. (2012) define a ratio of buoyancy fluxes due to along-front winds by Ekman transport and MLEs as

$$R^* = \tau_y \,/\, 0.06 \cdot \rho_0 \cdot b_{x.} \cdot MLD^2 \quad . \qquad [10]$$

The effects of restratification by MLEs and destratification by EBF are equal when R^*= 1. MLEs dominate submesoscale fluxes during restratification as winds stay lower than 0.06 N m^{-2}, which corresponds to the threshold where R^*= 1 assuming typical winter values of $b_x = 5 \cdot 10^{-8}$ s^{-2} and MLD = 100 m. Our findings suggest that spring restratification in the GoO is mainly induced by surface heating of the upper ocean, aided by a reduction in turbulent mixing caused by a weakening of wind strength and the positive contribution by MLEs. Our results suggest that the restratification timing may be conditioned by the presence of fronts (b_x) promoting MLEs and restratification via baroclinic instability. The presence of enhanced buoyancy fronts during spring 2016 may have led to an earlier restratification (by three weeks) relative to the previous year, when b_x was lower (Figure 7a).

4.3 Implications

The surface mixed layer is the window mediating between atmosphere and climate forcing, and the ocean interior, resulting in a coupling between MLD and the overall regional ecosystem (Kumar & Narvekar, 2005; Goes et al., 2020). A review of recent literature for the northern Arabian Sea, reveals evidence for certain climate-related changes to the atmosphere and ocean environment that directly impact the upper ocean and mixed layer processes presented in this study. Over multidecadal timescales, warming in the region is suggested to lead to gains in upper ocean stratification and stability, thereby reducing vertical mixing, primary production, and OMZ ventilation (Kumar et al., 2009; Piontkovski & Chiffings, 2014; Roxy et al., 2016; Parvathi et al., 2017; Lachkar et al., 2018, 2019). In contrast, studies focusing on mesoscale processes and episodic events suggest an opposing trend - the region shows increased rates of turbulent mixing caused by shifts in wind strength that increase the upwelling along the Arabian coasts (deCastro et al., 2016; Praveen et al., 2016, 2020) and an increase in Shamal wind events intensity over the last three decades (Aboobacker & Shanas, 2018). The increase in winds could counteract enhanced stratification induced by warming and may sustain the current mixing rates and modify advective pathways (Lachkar et al., 2020; Praveen et al., 2020).

Earth system models, such as those assessed by the Intergovernmental Panel on Climate Change, are conflicted on the climatic response of OMZs globally, with the predictions prone to low certainty and high variability on aspects such as the extent and magnitude of OMZs (Bopp et al., 2013; Oschlies et al., 2017, 2018). The major cause of uncertainty is the fact that coupled climate models do not resolve ocean processes smaller than their grid cells (10-100 km) (Lachkar et al., 2016). As an example, key processes associated with the meso- to submesoscale that have been observed in the region can drive enhanced overturning circulation that enhances vertical and horizontal motions, increasing vertical mixing, horizontal transport, and responses to net primary productivity (Chen et al., 2012; Banse et al., 2014; Lachkar et al., 2016; Queste et al., 2018; Johnson et al., 2019).

Our study and the glider datasets allow us to resolve these small-scale events and identify the significant impact of transient Q_L extreme events (driven by Shamals) and submesoscale processes on the MLD. We attempt to show their presence throughout the year but particularly in winter, when deeper MLDs (50-135 m) and therefore larger available potential energy lead to heightened submesoscale activity. Wintertime submesoscale restratifying fluxes are similar in magnitude to surface heat fluxes and thus play a major role in the surface buoyancy budget, emphasizing the need to better resolve and understand these processes and their role in the evolution of the surface ocean. Parameterizing submesoscale processes in one-dimensional ML models may modify the magnitude of stratification compared to when the model is only forced by surface fluxes, thereby altering ML dynamics and the physical-biological interaction in the region. Several studies have discussed the strong intraseasonal variability in primary productivity and carbon fluxes caused by transient mixing events or submesoscale fluxes in different regions (Swart et al., 2015; Lévy et al., 2018). For instance, the presence of submesoscale processes shown here suggests that they may be important in modeling net primary productivity during winter, as unlike many regions in the world, productivity in the GoO is comparatively large during this season. Moreover, they can be crucial in determining the timing of phytoplankton blooms and associated CO_2 flux, as spring restratification is synonymous with a subsurface bloom that persists throughout the intermonsoon season, potentially representing a significant carbon sink (Piontkovski et al., 2017).

In future scenarios of warming (IPCC et al., 2021), increase in stratification, and more intense wind events; we hypothesize that submesoscale processes, such as Q_{MLE}, may decrease due to reduced available potential energy in shallower MLDs, while Q_{EBF} would play a negligible role as its contribution might counterbalance. Overall, this would suggest a lesser impact of Q_{SMS} on surface ML. As Q_{SMS} are mostly restratifying the upper ocean in this region, our hypothesis would align with many of the regional studies stating it may not simply evolve to an increase in stratification and reduced primary productivity, and thus challenging the broad-scale statements on the future water column structure and OMZ evolution.

Our findings help to better understand the processes leading to stratification and mixing in the region, which have the potential to impact local biogeochemical cycling. However, our current glider datasets in the GoO are too short or at the wrong time of the year to, for example, understand the breakdown in stratification during autumn and the onset of stronger submesoscale energy in the periods of the year when the MLD is deep. We require additional observational campaigns, such as prolonged glider deployments observing at even high spatial resolution (< 3km) and occuring over all seasons to address future questions related to the rapidly evolving upper ocean physics and the associated response of biology (coupling to the OMZ and regional ecosystem). In addition, new glider sensors, such as ADCP and microstructure packages, are needed to elucidate the contribution of and relationship between wind stress and surface buoyancy forcing on upper ocean stratification and extent. These fine scale processes are likely to be important for ventilating and expanding the OMZ in a warming climate.

5 Conclusions

The seasonal evolution of the MLD and the restratification in the GoO is mainly driven by shortwave radiation, resulting in a positive net heat flux into the ocean. Q_{NET} is characterized by winter net heat loss and heat gain in spring due to an increase in Q_{SW}. Throughout winter, a deep ML (mean: 79±19 m) is present, owing to buoyancy loss caused primarily by net heat loss. During restratification, stable atmospheric conditions combined with heat entering the ocean are the driving forces behind the spring ML formation. The restratification timing is different by three weeks between years as a result of differences in the Q_{NET} cycle as well as weakening of wind forcing. Stronger incoming solar radiation during the spring intermonsoon causes buoyancy gain, increasing the stratification and shoaling the ML to 16±7 m on average. Wind-driven processes cause latent heat loss that promotes the submonthly MLD variability during both seasons. The primary drivers of Q_{L} are intense and dry northwesterly winds (Shamals), which are more frequent in winter than in spring. Submesoscale buoyancy fronts within the ML have the energy to restratify or mix the ML properties and have the potential to work against the general surface forcing fluxes at shorter time scales. Submesoscale fluxes represent 68% of overall positive buoyancy fluxes and primarily contribute to stratifying the winter upper ocean (11% of the time), highlighting how important they are in this region. They are present mainly during the formation of the spring ML, which may play a main role in determining the spring restratification timing.

Supporting Information

Supporting Information S1

Acknowledgments

This work was supported by the ONR GLOBAL grants N62909–14-1-N224/SQU and N62909-21-1-2008, Sultan Qaboos University grants EG/AGR/FISH/14/01 and IG/AGR/FISH/17/01, and UK NERC grants NE/M005801/1 and NE/N012658/1. We are grateful to the UEA Seaglider Facility, Sultan Qaboos University technical staff and Five Oceans Environmental Services consultancy for their technical help with instrument deployments and recoveries. SS is supported by a Wallenberg Academy Fellowship (WAF 2015.0186) and a Swedish Research Council grant (VR 2019-04400).

Data Availability Statement

The glider data are available from the British Oceanographic Data Centre (doi:10.5285/697eb954-f60c-603b-e053-6c86abc00062). ERA5 data are available at the Copernicus Climate Change Service (C3S) Climate Data Store: https: //cds.climate.copernicus.eu/cdsapp#!/dataset/reanalysis-era5-single-levels?tab=form.

References

Aboobacker, V. M., & Shanas, P. R. (2018). The climatology of shamals in the Arabian Sea—Part 1: Surface winds. *International Journal of Climatology*, *38*(12). https://doi.org/10.1002/joc.5711

Angel, M. (2017). Bathymetric distribution of Planktonic Ostracods (Ostracoda; Crustacea) in the Gulf of Oman (Northwest Indian Ocean) in relation to the Oxygen Minimum Zone. *International Journal of Marine Biology and Research*, *2*(1). https://doi.org/10.15226/24754706/2/1/00110

Banse, K., Naqvi, S. W. A., Narvekar, P. V., Postel, J. R., & Jayakumar, D. A. (2014). Oxygen Minimum Zone of the open Arabian Sea: Variability of oxygen and nitrite from daily to decadal timescales. *Biogeosciences*, *11*(8). https://doi.org/10.5194/bg-11-2237-2014

Boccaletti, G., Ferrari, R., & Fox-Kemper, B. (2007). Mixed layer instabilities and restratification. *Journal of Physical Oceanography*, *37*(9). https://doi.org/10.1175/JPO3101.1

Bopp, L., Resplandy, L., Orr, J. C., Doney, S. C., Dunne, J. P., Gehlen, M., Halloran, P., Heinze, C., Ilyina, T., Séférian, R., Tjiputra, J., & Vichi, M. (2013). Multiple stressors of ocean ecosystems in the 21st century: Projections with CMIP5 models. *Biogeosciences*, *10*(10). https://doi.org/10.5194/bg-10-6225-2013

CERC. (2002). Coastal Engineering Manual. *Coastal Engineering Manual*.

Chaichitehrani, N., & Allahdadi, M. N. (2018). Overview of wind climatology for the Gulf of Oman and the Northern Arabian Sea. *American Journal of Fluid Dynamics*, *8*(1).

Chen, G., Wang, D., & Hou, Y. (2012). The features and interannual variability mechanism of mesoscale eddies in the Bay of Bengal. *Continental Shelf Research*, *47*. https://doi.org/10.1016/j.csr.2012.07.011

D'Asaro, E., Lee, C., Rainville, L., Harcourt, R., & Thomas, L. (2011). Enhanced turbulence and energy dissipation at ocean fronts. *Science*, *332*(6027). https://doi.org/10.1126/science.1201515

deCastro, M., Sousa, M. C., Santos, F., Dias, J. M., & Gómez-Gesteira, M. (2016). How will Somali coastal upwelling evolve under future warming scenarios? *Scientific Reports*, *6*. https://doi.org/10.1038/srep30137

du Plessis, M., Swart, S., Ansorge, I. J., & Mahadevan, A. (2017). Submesoscale processes promote seasonal restratification in the Subantarctic Ocean. *Journal of Geophysical Research: Oceans*. https://doi.org/10.1002/2016JC012494 du Plessis, M., Swart, S., Ansorge, I. J., Mahadevan, A., & Thompson, A. F. (2019). Southern Ocean seasonal restratification delayed by submesoscale wind-front interactions. *Journal of Physical Oceanography*. https://doi.org/10.1175/JPO-D-18-0136.1

Eriksen, C. C., Osse, T. J., Light, R. D., Wen, T., Lehman, T. W., Sabin, P. L., Ballard, J. W., & Chiodi, A. M. (2001). Seaglider: A long-range autonomous underwater vehicle for oceanographic research. *IEEE Journal of Oceanic Engineering*, *26*(4). https://doi.org/10.1109/48.972073

EUMETSAT/OSI SAF. (2016). *MetOp-B AVHRR NAR SST data set. Ver. 1. Dataset accessed 2021-03-10 at https://doi.org/10.5067/GHGMB-3CO02*.

Fox-Kemper, B., Ferrari, R., & Hallberg, R. (2008). Parameterization of mixed layer eddies. Part I: Theory and diagnosis. *Journal of Physical Oceanography*, *38*(6). https://doi.org/10.1175/2007JPO3792.1

Garau, B., Ruiz, S., Zhang, W. G., Pascual, A., Heslop, E., Kerfoot, J., & Tintoré, J. (2011). Thermal lag correction on slocum CTD glider data. *Journal of Atmospheric and Oceanic Technology*, *28*(9). https://doi.org/10.1175/JTECH-D-10-05030.1

GEBCO. (2020). *GEBCO 2020 Grid. Dataset accessed 2021-02-15 at doi:10.5285/a29c5465-b138-234d-e053-6c86abc040b9*.

Giddy, I., Swart, S., Plessis, M. du, Thompson, A. F., & Nicholson, S.-A. (2021). Stirring of sea-ice meltwater enhances submesoscale fronts in the Southern Ocean. *Journal of Geophysical Research: Oceans*, *126*(4). https://doi.org/10.1029/2020jc016814

Goes, J. I., Tian, H., Gomes, H. do R., Anderson, O. R., Al-Hashmi, K., deRada, S., Luo, H., Al-Kharusi, L., Al-Azri, A., & Martinson, D. G. (2020). Ecosystem state change in the Arabian Sea fuelled by the recent loss of snow over the Himalayan-Tibetan Plateau region. *Scientific Reports*, *10*(1). https://doi.org/10.1038/s41598-020-64360-2

Hersbach, H., Bell, B., Berrisford, P., Hirahara, S., Horányi, A., Muñoz-Sabater, J., Nicolas, J., Peubey, C., Radu, R., Schepers, D., Simmons, A., Soci, C., Abdalla, S., Abellan, X., Balsamo, G., Bechtold, P., Biavati, G., Bidlot, J., Bonavita, M., … Thépaut, J. N. (2020). The ERA5 global reanalysis. *Quarterly Journal of the Royal Meteorological Society*, *146*(730). https://doi.org/10.1002/qj.3803

IPCC (2021). Climate Change 2021: The physical science basis. Contribution of working group I to the sixth assessment report of the Intergovernmental Panel on Climate Change. Masson-Delmotte, V., Zhai, P., Pirani, A., Connors, S. L., Péan, C., Berger, S., Caud, N., Chen, Y., Goldfarb, L., Gomis, M. I., Huang, M., Leitzell, K., Lonnoy, E., Matthews, J. B. R., Maycock, T. K., Waterfield, T., Yelekçi, O., Yu, R., & B, Z.. In *Cambridge University Press* (Issue In Press).

Johnson, K. S., Riser, S. C., & Ravichandran, M. (2019). Oxygen variability controls denitrification in the Bay of Bengal Oxygen Minimum Zone. *Geophysical Research Letters*, *46*(2). https://doi.org/10.1029/2018GL079881

Kumar, B. P., Cronin, M. F., Joseph, S., Ravichandran, M., & Sureshkumar, N. (2017). Latent heat flux sensitivity to sea surface temperature: Regional perspectives. *Journal of Climate*, *30*(1). https://doi.org/10.1175/JCLI-D-16-0285.1

Kumar, S. P., & Narvekar, J. (2005). Seasonal variability of the mixed layer in the central Arabian Sea and its implication on nutrients and primary productivity. *Deep-Sea Research Part II: Topical Studies in Oceanography*, *52*(14–15). https://doi.org/10.1016/j.dsr2.2005.06.002

Kumar, S. P., Roshin, R. P., Narvekar, J., Kumar, P. K. D., & Vivekanandan, E. (2009).

Response of the Arabian Sea to global warming and associated regional climate shift. *Marine Environmental Research*, *68*(5). https://doi.org/10.1016/j.marenvres.2009.06.010

Lachkar, Z., Lévy, M., & Smith, K. S. (2019). Strong intensification of the Arabian Sea Oxygen Minimum Zone in response to Arabian Gulf warming. *Geophysical Research Letters*, *46*(10). https://doi.org/10.1029/2018GL081631

Lachkar, Z., Lévy, M., & Smith, S. (2018). Intensification and deepening of the Arabian Sea Oxygen Minimum Zone in response to increase in Indian monsoon wind intensity. *Biogeosciences*, *15*(1). https://doi.org/10.5194/bg-15-159-2018

Lachkar, Z., Mehari, M., Azhar, M. A., Lévy, M., & Smith, S. (2020). Fast local warming of sea-surface is the main factor of recent deoxygenation in the Arabian Sea. *Biogeosciences*. https://doi.org/10.5194/bg-2020-325

Lachkar, Z., Smith, S., Lévy, M., & Pauluis, O. (2016). Eddies reduce denitrification and compress habitats in the Arabian Sea. *Geophysical Research Letters*, *43*(17). https://doi.org/10.1002/2016GL069876

Lévy, M., Franks, P. J. S., & Smith, K. S. (2018). The role of submesoscale currents in structuring marine ecosystems. *Nature Communications*, *9*(1). https://doi.org/10.1038/s41467-018-07059-3

Lévy, M., Shankar, D., André, J. M., Shenoi, S. S. C., Durand, F., & Montégut, C. de B. (2007). Basin-wide seasonal evolution of the Indian Ocean's phytoplankton blooms. *Journal of Geophysical Research: Oceans*, *112*(12). https://doi.org/10.1029/2007JC004090

L'Hegaret, P., Carton, X., Louazel, S., & Boutin, G. (2016). Mesoscale eddies and submesoscale structures of Persian Gulf Water off the Omani coast in spring 2011. *Ocean Science*, *12*(3). https://doi.org/10.5194/os-12-687-2016

Mahadevan, A., D'Asaro, E., Lee, C., & Perry, M. J. (2012). Eddy-driven stratification initiates North Atlantic spring phytoplankton blooms. *Science*. https://doi.org/10.1126/science.1218740

Mahadevan, A., Tandon, A., & Ferrari, R. (2010). Rapid changes in mixed layer stratification driven by submesoscale instabilities and winds. *Journal of Geophysical Research: Oceans*. https://doi.org/10.1029/2008JC005203

Matthews, A. J., Baranowski, D. B., Heywood, K. J., Flatau, P. J., & Schmidtko, S. (2014). The surface diurnal warm layer in the Indian ocean during CINDY/DYNAMO. *Journal of Climate*, *27*(24). https://doi.org/10.1175/JCLI-D-14-00222.1

Montégut, C. de B., Madec, G., Fischer, A. S., Lazar, A., & Iudicone, D. (2004). Mixed layer depth over the global ocean: An examination of profile data and a profile-based climatology. *Journal of Geophysical Research C: Oceans*, *109*(12). https://doi.org/10.1029/2004JC002378

Montégut, C. de B., Vialard, J., Shenoi, S. S. C., Shankar, D., Durand, F., Ethé, C., & Madec, G. (2007). Simulated seasonal and interannual variability of the mixed layer heat budget in the Northern Indian ocean. *Journal of Climate*, *20*(13). https://doi.org/10.1175/JCLI4148.1

Morvan, M., Carton, X., Corréard, S., & Baraille, R. (2020). Submesoscale dynamics in the Gulf of Aden and the Gulf of Oman. *Fluids*, *5*(3). https://doi.org/10.3390/fluids5030146

Niiler, P., & Kraus, E. (1977). One-dimensional models of the upper-ocean. Modeling and prediction of the upper layers of the ocean. *Pergamon*, 143–172.

Oschlies, A., Brandt, P., Stramma, L., & Schmidtko, S. (2018). Drivers and mechanisms of ocean deoxygenation. *Nature Geoscience*, *11*(7).

https://doi.org/10.1038/s41561-018-0152-2

Oschlies, A., Duteil, O., Getzlaff, J., Koeve, W., Landolfi, A., & Schmidtko, S. (2017). Patterns of deoxygenation: Sensitivity to natural and anthropogenic drivers. *Philosophical Transactions of the Royal Society A: Mathematical, Physical and Engineering Sciences*, *375*(2102). https://doi.org/10.1098/rsta.2016.0325

Parvathi, V., Suresh, I., Lengaigne, M., Izumo, T., & Vialard, J. (2017). Robust projected weakening of winter monsoon winds over the Arabian Sea under climate change. *Geophysical Research Letters*, *44*(19). https://doi.org/10.1002/2017GL075098

Piontkovski, S. A., & Chiffings, A. T. (2014). Long-term changes of temperature in the sea of Oman and the western Arabian Sea. *International Journal of Oceans and Oceanography*, *8*(1).

Piontkovski, S. A., & Queste, B. Y. (2016). Decadal changes of the Western Arabian sea ecosystem. *International Aquatic Research*, *8*(1). https://doi.org/10.1007/s40071-016-0124-3

Piontkovski, S. A., Queste, B. Y., Al-Hashmi, K. A., Al-Shaaibi, A., Bryantseva, Y. V., & Popova, E. A. (2017). Subsurface algal blooms of the northwestern Arabian Sea. *Marine Ecology Progress Series, 566*. https://doi.org/10.3354/meps11990

Pokhrel, S., Dutta, U., Rahaman, H., Chaudhari, H., Hazra, A., Saha, S. K., & Veeranjaneyulu, C. (2020). Evaluation of different heat flux products oover the tropical Indian Ocean. *Earth and Space Science*, *7*(6). https://doi.org/10.1029/2019EA000988

Pous, S. P. (2004). Hydrology and circulation in the Strait of Hormuz and the Gulf of Oman—Results from the GOGP99 Experiment: 2. Gulf of Oman. *Journal of Geophysical Research*, *109*(C12). https://doi.org/10.1029/2003jc002146

Praveen, V., Ajayamohan, R. S., Valsala, V., & Sandeep, S. (2016). Intensification of upwelling along Oman coast in a warming scenario. *Geophysical Research Letters*, *43*(14). https://doi.org/10.1002/2016GL069638

Praveen, V., Valsala, V., Ajayamohan, R. S., & Balasubramanian, S. (2020). Oceanic mixing over the northern arabian sea in a warming scenario: Tug of war between wind and buoyancy forces. *Journal of Physical Oceanography*, *50*(4). https://doi.org/10.1175/JPO-D-19-0173.1

Price, J. F., Mooers, C. N. K., & Van, J. C. L. (1978). Observation and simulation of storm-induced mixed-layer deepening. *Journal of Physical Oceanography*, *8*(4, Jul.1978). https://doi.org/10.1175/1520-0485(1978)008<0582:oasosi>2.0.co;2

Queste, B. Y., Vic, C., Heywood, K. J., & Piontkovski, S. A. (2018). Physical controls on oxygen distribution and denitrification potential in the North West Arabian Sea. *Geophysical Research Letters*, *45*(9). https://doi.org/10.1029/2017GL076666

Reynolds, R. M. (1993). Physical oceanography of the Gulf, Strait of Hormuz, and the Gulf of Oman-Results from the Mt Mitchell expedition. *Marine Pollution Bulletin*, *27*(C). https://doi.org/10.1016/0025-326X(93)90007-7

Rixen, T., Cowie, G., Gaye, B., Goes, J., Gomes, H. do R., Hood, R., Lachkar, Z., Schmidt, H., Segschneider, J., & Singh, A. (2020). Present past and future of the OMZ in the northern Indian Ocean. *Biogeosciences Discussions*. https://doi.org/10.5194/bg-2020-82

Roxy, M. K., Modi, A., Murtugudde, R., Valsala, V., Panickal, S., Kumar, S. P., Ravichandran, M., Vichi, M., & Lévy, M. (2016). A reduction in marine primary productivity driven by rapid warming over the tropical Indian Ocean. *Geophysical Research Letters*, *43*(2). https://doi.org/10.1002/2015GL066979

Sabine, C. L., Feely, R. A., Gruber, N., Key, R. M., Lee, K., Bullister, J. L., Wanninkhof, R., Wong, C. S., Wallace, D. W. R., Tilbrook, B., Millero, F. J., Peng, T. H., Kozyr, A., Ono, T., & Rios, A. F. (2004). The oceanic sink for anthropogenic CO2. *Science*, *305*(5682). https://doi.org/10.1126/science.1097403

Schmidt, H., Czeschel, R., & Visbeck, M. (2019). Ventilation dynamics of the Oxygen Minimum Zone in the Arabian Sea. *Biogeosciences Discussions*. https://doi.org/10.5194/bg-2019-168

Senafi, F. A., Anis, A., & Menezes, V. (2019). Surface heat fluxes over the northern Arabian Gulf and the northern Red Sea: Evaluation of ECMWF-ERA5 and NASA-MERRA2 reanalyses. *Atmosphere*, *10*(9). https://doi.org/10.3390/atmos10090504

Suneet, D., Kumar, M. A., & Atul, S. (2019). Upper ocean high resolution regional modeling of the Arabian Sea and Bay of Bengal. *Acta Oceanologica Sinica*, *38*(5). https://doi.org/10.1007/s13131-019-1439-x

Swart, S., Plessis, M. D. du, Thompson, A. F., Biddle, L. C., Giddy, I., Linders, T., Mohrmann, M., & Nicholson, S. A. (2020). Submesoscale fronts in the Antarctic Marginal Ice Zone and their response to wind forcing. *Geophysical Research Letters*, *47*(6). https://doi.org/10.1029/2019GL086649

Swart, S., Thomalla, S. J., & Monteiro, P. M. S. (2015). The seasonal cycle of mixed layer dynamics and phytoplankton biomass in the Sub-Antarctic Zone: A high-resolution glider experiment. *Journal of Marine Systems*, *147*. https://doi.org/10.1016/j.jmarsys.2014.06.002

Thomas, L. N. (2005). Destruction of potential vorticity by winds. *Journal of Physical Oceanography*, *35*(12). https://doi.org/10.1175/JPO2830.1

Thomas, L. N., & Lee, C. M. (2005). Intensification of ocean fronts by down-front winds. *Journal of Physical Oceanography*, *35*(6). https://doi.org/10.1175/JPO2737.1

Thompson, A. F., Lazar, A., Buckingham, C., Garabato, A. C. N., Damerell, G. M., & Heywood, K. J. (2016). Open-ocean submesoscale motions: A full seasonal cycle of mixed layer instabilities from gliders. *Journal of Physical Oceanography*, *46*(4). https://doi.org/10.1175/JPO-D-15-0170.1

Turner, J. S. (1973). *Buoyancy effects in fluids.* https://doi.org/10.1017/cbo9780511608827

Vic, C., Roullet, G., Capet, X., Carton, X., Molemaker, M. J., & Gula, J. (2015). Eddy-topography interactions and the fate of the Persian Gulf Outflow. *Journal of Geophysical Research: Oceans*. https://doi.org/10.1002/2015JC011033

Viglione, G. A., Thompson, A. F., Flexas, M. M., Sprintall, J., & Swart, S. (2018). Abrupt transitions in submesoscale structure in Southern Drake Passage: Glider observations and model results. *Journal of Physical Oceanography*, *48*(9). https://doi.org/10.1175/JPO-D-17-0192.1

Yu, L. (2009). Sea surface exchanges of momentum, heat, and fresh water determined by satellite remote sensing. In *Encyclopedia of Ocean Sciences*. 10.1016/B978-012374473-9.00800-6

AGU PUBLICATIONS

Journal of Geophysical Research: Oceans

Supporting Information for

Seasonal to intraseasonal variability of the surface mixed layer in the Gulf of Oman

Estel Font [1], Bastien Y. Queste[1], and Sebastiaan Swart[1,2]

[1] Department of Marine Sciences, University of Gothenburg, Gothenburg, Sweden, [2]Department of Oceanography, University of Cape Town, Rondebosch, South Africa

Contents of this file

Figure S1

Introduction

The supporting information contains an additional figure. We provide a supporting figure to validate the glider data management. Seaglider 579 was deployed in March 2015 until the end of May 2015 (91 days) during the spring intermonsoon and Seaglider 510 was deployed in mid-December 2015 and recovered at the end of March 2016 (108 days) during the winter NW monsoon. The data shows the bias between the up and downcast of the corrected glider data profiles for each season. There is an evident deviation during both seasons in the measurements at the first meters of the downcast profiles, more prominent during spring. The temperature bias is caused by the warming of the sensors during the communication phase at the surface between dives. Strong solar radiation warmed the glider and its sensors, causing an artificial rise in potential temperature. The bias in the downcast profiles produces fictitious results when observing lateral gradients, hence only climb profiles are used in this study.

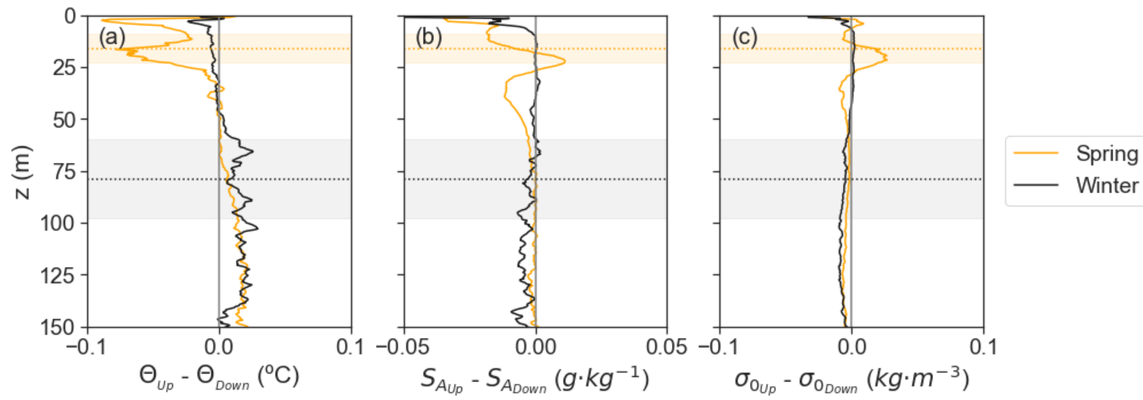

Figure S1. Temperature bias between up and downcast profiles. (a) Conservative temperature (Θ), (b) absolute salinity (S_A), and (c) potential density (σ_0) bias between up and downcast corrected data profiles for each season. The average MLD is displayed as the horizontal dotted line and the shading shows the STD. High air temperatures in the region cause warming of the sensors during the communication phase at the surface producing a bias in the measurements at the first meters of the downcast profiles. The deviation is evident during both seasons, although it is more prominent during spring when solar radiation is stronger.